

Studying disorder in graphite-based systems by Raman spectroscopy†

M. A. Pimenta,^a G. Dresselhaus,^b M. S. Dresselhaus,^{cd} L. G. Cançado,^{‡a}
A. Jorio^a and R. Saito^e

Received 25th September 2006, Accepted 7th December 2006

First published as an Advance Article on the web 11th January 2007

DOI: 10.1039/b613962k

Raman spectroscopy has historically played an important role in the structural characterization of graphitic materials, in particular providing valuable information about defects, stacking of the graphene layers and the finite sizes of the crystallites parallel and perpendicular to the hexagonal axis. Here we review the defect-induced Raman spectra of graphitic materials from both experimental and theoretical standpoints and we present recent Raman results on nanographites and graphenes. The disorder-induced *D* and *D'* Raman features, as well as the *G'*-band (the overtone of the *D*-band which is always observed in defect-free samples), are discussed in terms of the double-resonance (DR) Raman process, involving phonons within the interior of the 1st Brillouin zone of graphite and defects. In this review, experimental results for the *D*, *D'* and *G'* bands obtained with different laser lines, and in samples with different crystallite sizes and different types of defects are presented and discussed. We also present recent advances that made possible the development of Raman scattering as a tool for very accurate structural analysis of nano-graphite, with the establishment of an empirical formula for the in- and out-of-plane crystalline size and even fancier Raman-based information, such as for the atomic structure at graphite edges, and the identification of single *versus* multi-graphene layers. Once established, this knowledge provides a powerful machinery to understand newer forms of sp² carbon materials, such as the recently developed pitch-based graphitic foams. Results for the calculated Raman intensity of the disorder-induced *D*-band in graphitic materials as a function of both the excitation laser energy (E_{laser}) and the in-plane size (L_a) of nano-graphites are presented and compared with experimental results. The status of this research area is assessed, and opportunities for future work are identified.

1. Introduction

The scientific interest in graphite was recently stimulated by the report of the massless and relativistic properties of the conduction electrons in a single graphene layer responsible for the unusual properties of the quantum Hall effect in this system.^{1,2} The study of the fundamental physical properties of graphite is essential for understanding the properties of new nanostructured sp² carbon forms, such as graphenes, fullerenes and carbon nanotubes.⁵ The characterization of these materials is essential, especially from an applications point of view. Many groups are now making devices using graphene

ribbons with a long length and small width, where edge defects play an important role. Thus, the investigation of defects and stacking disorder has now become an important issue for the future development of graphite-based nanostructures in device applications.

Raman spectroscopy has historically played an important role in the structural characterization of graphitic materials,^{4,5} and has been widely used in the last four decades to characterize graphitic systems, such as pyrolytic graphite, carbon fibers,⁴ glassy carbon, nanographite ribbons,⁶ fullerenes and carbon nanotubes.³ Basic structural properties, such as in-plane crystallite size^{7,8} and out-of-plane stacking order^{9–11} have been shown to strongly affect the Raman spectra of graphite. However, quantitative analysis was lacking, basically due to poor sample quality. When going towards micro- and nanometer sized graphitic materials, amorphization takes place, substantially increasing the sp³ carbon sample content, leading to significant changes in the Raman profiles.¹² However, recent systematic studies have made possible the development of Raman scattering as a tool for very accurate structural analysis of nano-graphite, with the establishment of an empirical formula for the in- and out-of-plane crystalline size dependence of the Raman scattering intensity^{13,14} and even fancier Raman-based information sensitive to the atomic structure at graphite edges,¹⁵ the anisotropy in the optical

^a Departamento de Física, Universidade Federal de Minas Gerais, Belo Horizonte-MG, 30123-970, Brazil

^b Francis Bitter Magnet Laboratory, Massachusetts Institute of Technology, Cambridge, MA, 02139-4307, USA

^c Department of electrical Engineering and Computer Science, Massachusetts Institute of Technology, Cambridge, MA, 02139-4307, USA

^d Department of Physics, Massachusetts Institute of Technology, Cambridge, MA, 02139-4307, USA

^e Department of Physics, Tohoku University and CREST, Sendai, 980-8578, Japan

† The HTML version of this article has been enhanced with colour images.

‡ Present address: Institute of Optics, University of Rochester, NY, 14627-0171.

absorption of graphite ribbons⁶ and the identification of single *versus* multi-graphene layers.^{16–18} Once established, this fundamental knowledge provides powerful machinery to understand newer forms of practical sp^2 carbon materials, such as the recently developed pitch-based graphitic foams, that due to its mixed two-dimensional/three-dimensional aspect, have a very high thermal conductivity to weight ratio.^{19,20}

Although measuring Raman spectra from nanostructured sp^2 carbons is not difficult using current technology, to get detailed information from such spectra requires some background in the Raman spectra for graphite. The present review is aimed at helping the user community of graphitic materials to understand how to characterize their materials by Raman spectroscopy with particular emphasis given to the spectral features induced by disorder, *e.g.*, the *D*-band. In section 2, we give an overview of the structure and phonons in sp^2 carbon-based materials, some of the different types of common defects, and the disorder-induced features in the Raman spectra that are used to probe these defects. In section 3, the theoretical basis of disorder-induced Raman scattering is reviewed, and we discuss the double resonance Raman mechanism. In section 4, experimental results are presented, with particular emphasis given to systematic studies of the Raman spectra associated with specific defects. A method for calculation of the *D*-band Raman spectra is then discussed in section 5, including the calculation of the optical matrix elements, the electron phonon-interaction and the calculated *D*-band intensities *vs.* laser energy and crystallite size. In section 6, a summary and an outlook toward future research opportunities for this topic are given.

2. Overview

2.1. Structure and phonons in graphite

2.1.1. sp^2 covalent bonding. Graphite is a 3-D layered material formed by stacking single graphene layers of 2-D graphite. Graphite consist of sp^2 carbon hexagonal networks of carbon atoms with covalent bonding between C atoms within a plane and a weak van der Waals interaction between planes. Since the sp^2 covalent bond is strong, the melting temperature of graphite is the highest among materials (more than 4300 °C),²¹ and annealing of the crystal usually requires more than 2300 °C to establish 3-D interlayer AB stacking (the Bernal structure). Even with high temperature heat treatment,

a truly single crystal of graphite is hardly ever obtained. Thus, all graphite materials have some defects in practice, and different types of materials have different types of defects. Defects give rise to a variety of special practical applications, such as enhanced mechanical strength, electrical conductivity, energy storage capacity for battery applications, to mention a few examples.

2.1.2. Phonon dispersion of graphite. To interpret their Raman spectra, understanding the phonon dispersion of graphite is essential. In 2-D graphite, there are two carbon atoms per unit cell, and thus six phonon dispersion relations are obtained (see Fig. 1a), in which three of the six phonon modes are acoustic (A) and the other three are optic (O) phonon modes. For the three acoustic and three optic phonon modes, one is an out-of-plane (oT) phonon mode and the other two are in-plane modes, one longitudinal (L) and the other one transverse (iT). As a result, starting from the highest energy at the Γ point, the six phonon dispersion curves are assigned to LO, iT, oT, LA, iT, and oTA phonon modes. In the case of graphite, the LO and iT phonon modes are degenerate at the Γ point. The phonon mode frequencies of graphite have been recently observed by inelastic X-ray scattering,²³ as shown in Fig. 1b. Group theory tells us that the degenerate LO and iT phonon mode (E_{2g} symmetry) at the Γ point is Raman active, while the oT phonon mode is infrared active.^{3,24}

The degeneracy of the LO and iT phonons disappears for general points inside the first Brillouin zone (BZ) of graphite. As shown in Fig. 1b, along the Γ -K line, the LO and iT branches will have T_3 and T_1 symmetries, respectively, whereas the symmetries of these branches along the Γ -M line are Σ_1 and Σ_3 , respectively. Exactly at the K-point, the phonon which comes from the iT branch is non degenerate and belongs to the A_1' irreducible representation of the point group D_{3h} . The LO and LA phonon branches meet each other at the K point giving rise to a doubly degenerate phonon, with E' symmetry.^{23,25}

Finally, to correctly describe the dispersion of the LO and TO phonon branches near the Γ and K points, it is important to consider the coupling of electrons and phonons²² leading to an interesting effect known as the Kohn anomaly.²⁶ The Kohn anomaly is responsible for a softening of selected Γ and K point phonons, thus increasing the phonon dispersion near these points in the BZ. As will be shown later, important

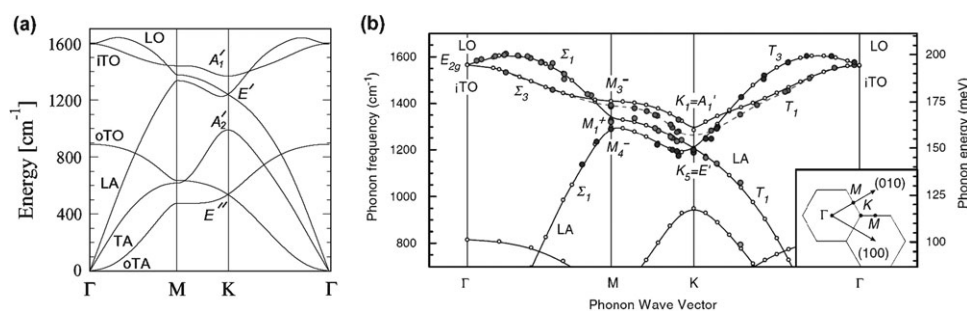


Fig. 1 (a) Calculated phonon dispersion relations of two dimensional graphite.²² LO, iT, oT, LA, TA and oTA are phonon modes at the Γ point and A_1' , E' , A_2' , and E'' are irreducible representations for phonon modes at the K point. (b) Inelastic X-ray measurements of phonon dispersion relations of graphite.²³

defect-induced Raman features originate from these phonons and their properties reflect the Kohn anomaly.

2.2. Defects and their observations

Defects in graphitic materials are important for improving the performance of carbon-based materials for practical applications. Because of the high anisotropy of the mechanical strength or the electrical conductivity between the in-plane and out-of-plane directions, defects often improve the performance of carbon materials. For example, to avoid the slip of the graphitic plane with respect to its neighbors, orientational disorder of the graphite planes is useful, and it is essential for enhancing the average isotropic mechanical strength. We will discuss below the different kinds of defects that can at present be characterized by Raman spectroscopy.

2.2.1. Stacking faults. The hexagonal network of graphite layers is stacked in the direction perpendicular to the layer plane (*c*-axis) in an AB stacking arrangement in which the vacant centers of the hexagons on one layer have carbon atoms on hexagonal corner sites on the two adjacent graphene layers. In turbostratic graphite there is no stacking order between adjacent layers and the interlayer space (>0.342 nm) is larger than that for crystalline graphite (0.335 nm). Reducing the stacking faults is important for reducing the friction of graphitic materials.

In graphite with AB stacking, the unit cell consists of four carbon atoms and there are two bonding and two anti-bonding π bands which are split at the Γ point of the BZ by an interlayer interaction denoted by γ_1 .²⁷ In 3D graphite, there is an energy dispersion along the *c* direction perpendicular to the plane, while for a finite number of graphene planes, we have several 2-D energy bands split by discrete *k* vectors in the *c* direction. If there is incommensurate stacking, the resulting material can be treated as a 2-D graphite, but in the real case, we need to consider a more realistic electronic structure.

2.2.2. Crystallite size. Actual graphitic materials are, in general, poly-crystalline, with a crystallite size that can be controlled by heat treatment. By increasing the heat treatment temperature T_{ht} (in the range 1000–2900 °C) and the duration time (1–48 h) of the heat treatment of a polymer-derived precursor, such as polyparaphenylene (PPP)²⁸ or polyacrylonitrile (PAN),²⁹ the crystallite size, mainly the in-plane crystallite size L_a , increases. Since the electrical resistivity arises in part from the hopping of carriers between crystallites in the sample, increases in the crystallite size reduces the resistivity. Ions are intercalated between two layers to form a graphite intercalation compound (GIC)³⁰ which is an important material for secondary batteries, such as lithium ion batteries.^{31,32} A large crystallite size is important for obtaining a reproducible high capacity for such batteries, though the crystallite size can be reduced after many charge-discharge cycles because of the relative motion of adjacent graphitic planes. After about 100 charge-discharge cycles, the battery capacity is reduced significantly unless carbon nanotube additives are used to maintain dimensional stability.²⁸

2.2.3. Edge states. An edge of a small graphite cluster or a nanographite sample has revealed some exotic physics related

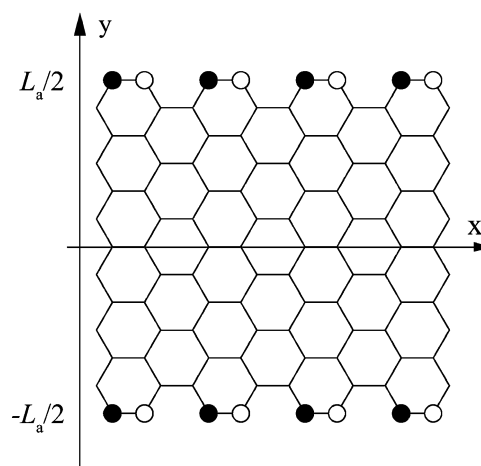


Fig. 2 The model of a nanographite ribbon with the armchair edge at $y = \pm L_a/2$ and zigzag edge along *y* axis. In the armchair edge, we have two carbon atoms (solid and open circles) which belong to different sublattices A and B of graphite. Edge states exist only in the zigzag edges.³³

to edge states. The two basic kinds of edge structures in nanographite are shown in Fig. 2 with the armchair edge along the *x*-axis or the zigzag edge along the *y*-axis. In the unit cell of graphite, we have two carbon atoms A and B which give rise to two sublattices. In an armchair edge, there are two distinct carbon atoms for the two different sublattices. For the zigzag edge, only carbon atoms on a single sublattice appear. Because of the lack of symmetry between the A and B sublattices, localized electronic states appear around the zigzag edge, while no edge states appear for armchair edges.³³ Thus, the energy dispersion in the direction of the edge is flat for zigzag edges, and a sharp maximum appears in the density of states at the Fermi energy, and these effects are widely discussed in the context of magnetism.³⁴ The observation of the special properties of selected types of edge states is commonly done using scanning tunneling spectroscopy (STS)^{35,36} and micro-Raman spectroscopy.⁶

2.3. Raman scattering in graphitic materials

2.3.1. The G-band and the disorder-induced D and D' bands. Since all graphitic materials are black in color with a similar density, the characterization of graphitic samples to distinguish one from another is important. Before making mechanical tests, conductivity or other electrical measurements, it is common to carry out standard characterization measurements on sp^2 graphitic materials, which include Raman spectroscopy along with X-ray, SEM and TEM for structural evaluation. Raman spectroscopy is a relatively easy, non-destructive, non-contacting, and quick measurement method to probe the inelastic scattering of light from a sample surface at room temperature at ambient pressure.

The most prominent features in the Raman spectra of graphitic materials (see for example, Fig. 3) are the so-called G band appearing at 1582 cm^{-1} (graphite), the D band^{7,8} at about 1350 cm^{-1} , the D'-band at about 1620 cm^{-1} and the G'-band at about 2700 cm^{-1} (for these three last bands, the given

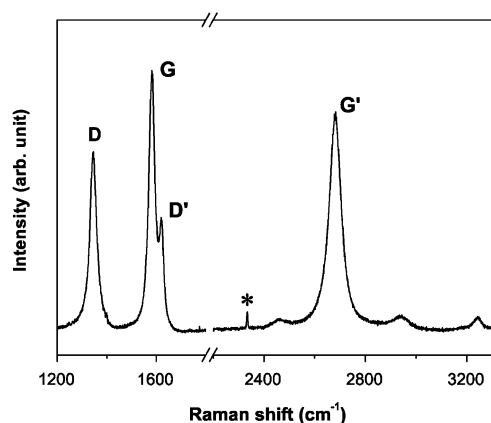


Fig. 3 Raman spectrum of a nanographite sample, showing the main Raman features, the *D*, *G*, *D'* and *G'* bands taken with a laser excitation energy (wavelength) of 2.41 eV (514.5 nm). The peak with * comes from the Raman mode of N₂ gas (~ 2330 cm⁻¹) present in the air surrounding the sample. Other less intense Raman features from graphite are just not labelled here, but they have been assigned elsewhere.⁵

Raman frequency is that obtained using the laser excitation wavelength at 514.5 nm). The *G* band is a doubly degenerate (iTO and LO) phonon mode (E_{2g} symmetry) at the BZ center that is Raman active for sp^2 carbon networks. If we see the *G* band in the Raman spectra, we can say that the sample contains sp^2 carbon networks. In contrast, sp^3 and sp carbon networks show characteristic Raman features at 1333 cm⁻¹ (diamond^{37,38}) and in the range 1850 – 2100 cm⁻¹ (linear carbon chains^{39–41}), respectively. The *D* and *D'* bands are defect-induced Raman features, and thus these bands cannot be seen for a highly crystalline graphite. The integrated intensity ratio I_D/I_G for the *D* band and *G* band is widely used for characterizing the defect quantity in graphitic materials.

The disorder-induced character of the *D* band is clearly observed in Fig. 4 which shows two confocal Raman images of a $6\ \mu\text{m}$ highly oriented pyrolytic graphite crystallite deposited on a glass substrate. Fig. 4a shows a Raman image of the crystallite, plotting the spatial dependence of the *G* band intensity. In Fig. 4b the intensity of the disorder-induced *D* band is shown. Fig. 4c shows two Raman spectra, one at the interior of the crystallite, and the other at the edge. It is clear from Fig. 4a–c that the *G* band intensity is uniform over the

whole graphite surface, while the *D*-band intensity is localized where the crystalline structure is not perfect, mostly at the edges of the crystallite.

2.3.2. The second-order *G'*-band. All kinds of graphitic materials exhibit a strong Raman band which appears in the range 2500 – 2800 cm⁻¹ (see Fig. 3) and this feature corresponds to the overtone of the *D* band. Since this band is symmetry-allowed and appears in the second-order Raman spectra of crystalline graphite (without any kind of disorder), it was originally called the *G'* band. Other authors prefer to call it the $2D$ or D^* band, since it corresponds to the overtone of the *D* band. In this article, we will use the conventional notation (*G'*-band), considering that it is the second most intense feature in the Raman spectrum of the completely ordered 3D graphite, and to avoid confusion between the designation of this feature and the use of $2D$ to denote two dimensionality. The Raman feature at about 2950 cm⁻¹ in Fig. 3 is associated with a $D + G$ combination mode and also is induced by disorder.

2.3.3. Crystallite size dependence of the *D*-band. In 1970, Tuinstra and Koenig^{7,8} performed systematic Raman and X-ray diffraction studies of many graphitic samples with different in-plane crystallite sizes L_a , and concluded that the ratio of the *D* and *G* band intensities (I_D/I_G) is inversely proportional to the in-plane crystallite sizes L_a , which were obtained from the width of the X-ray diffraction peaks. After this pioneering work, the ratio I_D/I_G was used for many years to estimate L_a in disordered carbon materials. Knight and White⁴³ later summarized the Raman spectra of various graphitic systems measured using the $\lambda = 514.5$ nm ($E_{\text{laser}} = 2.41$ eV) laser line and derived an empirical expression which allows the determination of L_a from the (I_D/I_G) ratio.⁴³ A general formula giving L_a of nano-graphite systems for any excitation laser energy in the visible range is presented in Section 4.1.¹³

2.3.4. Dimensionality dependence of the *G'*-band. Raman spectroscopy can be used to quantify the structural parameters along the *c* axis, since the *G'* band, the second-order of the *D* band, is very sensitive to the stacking order of the graphene sheets along the *c* axis.^{9–11} Nemanich and Solin were the first to show the change from one peak to two peaks in the profile of the *G'* band in the Raman spectra obtained from

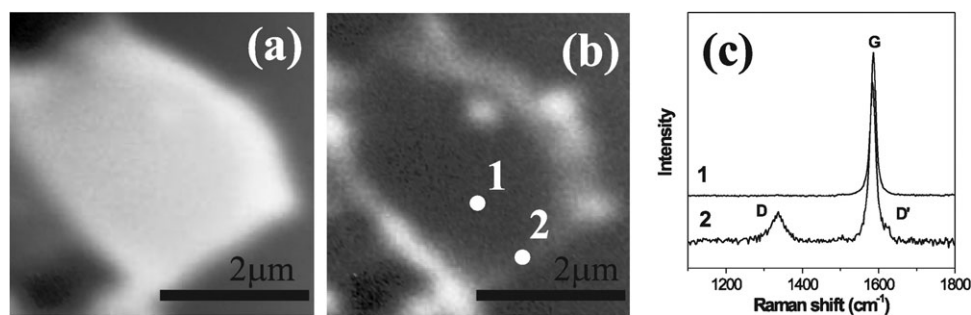


Fig. 4 (a) *G* band and (b) *D* band confocal (400 nm resolution) Raman images of a graphite crystallite deposited on a glass substrate. (c) The Raman spectra obtained in regions 1 and 2 (white circles) depicted in panel (b) are shown. The excitation comes from a HeNe ($\lambda = 633$ nm) laser. See ref. 42 for experimental setup description.

polycrystalline graphite and crystalline graphite, respectively.^{44,45} Lespade *et al.*^{9,10} performed a Raman spectroscopy study in carbon materials heat treated at different temperatures T_{htt} and observed that, by increasing T_{htt} , the G' band changes from a one peak to a two peak feature. They associated this evolution with the degree of graphitization of the samples and suggested that the origin of the two-peak structure of the G' band in crystalline graphite was related to the stacking order occurring along the c axis. Recently, the evolution of the G' band from a single to a few graphene layers,^{16–18} and its complete evolution from the 2-D to 3-D aspect (from one to two peaks) have been quantitatively systematized,¹⁴ as discussed further in section 4.1. Furthermore, Barros *et al.* have used the G' band to identify three G' band peaks due to the coexistence of 2-D and 3-D graphite phases in pitch-based graphitic foams.²⁰

2.3.5. Dispersive behavior of the D -band and G' -band. The physical origin of the disorder-induced D -band was initially discussed in terms of a maximum in the phonon density of states (PDOS) but, in 1981, Vidano *et al.*⁴⁶ showed that the D -band has a dispersive behavior whereby the D band frequency ω_D changes with the energy of the incident laser, E_{laser} , revealing that the physical origin of this band could not be related to a maximum in the PDOS. Vidano *et al.*⁴⁶ performed a systematic investigation of the Raman spectra of different kinds of carbon materials as a function of E_{laser} and they observed that ω_D upshifts with increasing E_{laser} in a linear way over a wide laser energy range, the slope of $(\Delta\omega_D/\Delta E_{\text{laser}})$ being about $50 \text{ cm}^{-1}/\text{eV}$. After this work, the dependence of ω_D on E_{laser} was observed in many different sp^2 carbon materials, including carbon black⁴⁷ a-C materials,⁴⁸ pyrolytic graphites,⁴⁹ carbon nanotubes,⁵⁰ disordered graphite⁵¹ and in graphite edges⁵² and the slope of $(\Delta\omega_D/\Delta E_{\text{laser}})$ was observed to be almost independent of the material type. It was also observed in these works that the G' -band, which is the overtone of the D -band, also exhibits a dispersive behavior, the slope of $(\Delta\omega_{G'}/\Delta E_{\text{laser}})$ being about $100 \text{ cm}^{-1}/\text{eV}$ (two times the slope of the D -band).

A dispersive behavior is observed not only for the D and G' , but also for the D' and for many other low intensity features

observed at different frequencies in the Raman spectra of graphite.⁵³ They are all related to different phonon branches in the interior of the BZ that are activated in first-order scattering by defects. Interestingly, these features and their E_{laser} dependence can be used to measure the phonon dispersion of graphite materials with light scattering.⁵³ In section 3, we focus our attention on the physical origin of the disorder-induced bands in graphite and their dispersive behavior.

3. Double resonance Raman processes

The first successful attempt to explain the origin and the dispersive behavior in the frequency of the D and G' bands was presented by Baranov *et al.*,⁵⁴ who proposed that the D and G' bands in graphite originated from a double resonance (DR) Raman process. This concept was further developed by Thomsen and Reich,⁵⁵ who calculated the scattering cross section for the double resonance mechanism that gives rise to the D band. It was also shown in this work⁵⁵ that the wavevectors q of the phonons associated with the D band (measured from the k point) would couple preferentially to the electronic states with wavevectors k (measured from the K point) such that $q = 2k$. Saito *et al.*⁵³ generalized the concept of the D -band double resonance mechanism in graphite, and showed that it can be used to probe all phonon branches of graphite near the Γ and K points of the graphite 2-D BZ. Moreover, it was shown that the D band originated from an intervalley DR process, involving electronic states around two inequivalent K points in the BZ of graphite, whereas the D' band, which appears in the Raman spectrum at around 1620 cm^{-1} , originated from an intravalley DR process involving electronic states around the same K point.⁵³

Here we summarize the theory of the scattering processes associated with the D -band, D' -band and the G' -band features of the Raman spectra. Calculations based on this theory are reviewed in section 5. In second-order DR (double resonance) Raman processes for sp^2 carbon materials (see Fig. 5b and c), the electron (1) absorbs a photon at a k state, (2) scatters to $k + q$ states, (3) scatters back to a k state, and (4) emits a photon by recombining with a hole at a k state. Therefore, in a DR Raman process, two resonance conditions for three

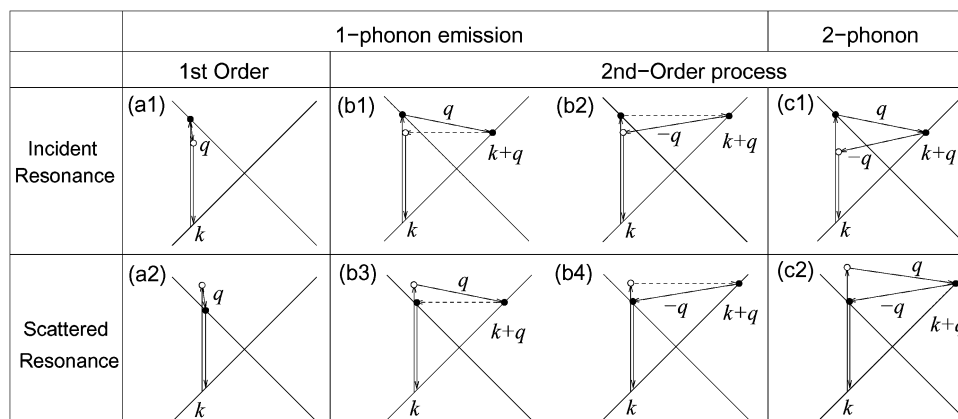


Fig. 5 (a) First-order and (b) one-phonon second-order, (c) two-phonon second order resonance Raman spectral processes.⁵ (top) incident photon resonance and (bottom) scattered photon resonance conditions. For one-phonon, second-order transitions, one of the two scattering events is an elastic scattering event (dashed lines). Resonance points are shown as solid circles. See text for details.

intermediate states should be satisfied, in which the intermediate $\mathbf{k} + \mathbf{q}$ state is always a real electronic state and either the initial or the final \mathbf{k} state is a real electronic state.

In the case of the *D*-band and *D'*-band, the two scattering processes consist of one *elastic* scattering event by defects of the crystal and one *inelastic* scattering event by emitting or absorbing a phonon, as shown in Fig. 5b. In the case of the *G'*-band, both processes are *inelastic* scattering events involving two phonons. Thus, both (1) one-elastic and one-inelastic scattering event (Fig. 5b) and (2) two-inelastic scattering events (Fig. 5c) can be considered as second-order Raman processes. Hereafter we call the resulting spectral features, respectively, one-phonon and two-phonon double resonance Raman bands.⁵⁶

The electronic structure of 2-D graphite near the Fermi energy is linear in wave vector k , which is expressed by the crossed solid lines in Fig. 5.³ The crossing point corresponds to the Fermi energy located at the *K* point. When E_{laser} is increased, the resonance k vector for the electron moves away from the *K* point. In the DR process, the corresponding q vector for the phonon increases with increasing k , as measured from the *K* point. Thus by changing the laser energy, we can observe the phonon energy $\hbar\omega(q)$ along the phonon dispersion relations (Fig. 1). This effect is observed experimentally as a dispersion of the phonon energy as a function of E_{laser} .⁵⁶ A tunable laser system can directly show this dispersive behavior for the *D*-band, *D'*-band and *G'*-band in the Raman spectrum.

The difference between the DR process for the *D* and *D'* bands is that, for the *D*-band the \mathbf{k} and $\mathbf{k} + \mathbf{q}$ states are around two inequivalent *K* points (*K* and *K'*) at the corners of the Brillouin zone and this situation corresponds to an inter-valley DR process. The phonons associated with this process have a large wavevector, which is in the vicinity of the *K* point. For the *D'*-band, the \mathbf{k} and $\mathbf{k} + \mathbf{q}$ states are around the same *K* (or *K'*) point. This is an intra-valley process and the associated phonons have small wavevectors which are in the vicinity of the Γ point.⁵³

The initial (or final) \mathbf{k} and the intermediate $\mathbf{k} + \mathbf{q}$ states exist on equi-energy contours of the electronic structure. A low energy equi-energy contour of graphite is a circle around the *K*

point in the 2D BZ (see Fig. 6) if we neglect the trigonal warping effect.^{56a} As a result, the possible \mathbf{q} states are on circles which we rotate around Γ (or the *K* point). In this case, the density of states for possible \mathbf{q} states becomes singular for $q \approx 0$ and $q \approx 2k$.^{53,57} However, there is only one resonance peak corresponding to the $q \approx 2k$ condition, since the peak at $q \approx 0$ is absent (or very weak) because the electron-phonon coupling for this situation is null at the *K* point.⁵³

It is important to comment that we here consider only scattering of electrons by phonons. However, the Raman process can occur by scattering of holes. In the special case of graphite, where the valence and conduction bands are almost symmetrical, this can lead to an important effect that has not been discussed, that is the triple-resonance process. For example, by looking at Fig. 5c1, we can consider that, instead of the electron being scattered back by a phonon with $-q$, the hole will be scattered instead. In this case, the electron-hole generation is a resonant process, both electron and hole scattering will be resonant, and finally the electron-hole recombination at the opposite side with respect to the *K* point will also be resonant, leading to a triple-resonance process. This possibility might explain why the *G'*-band is as intense as the allowed first-order *G*-band in the Raman spectra of graphitic materials and even more intense than the *G* band in single layer graphene.¹⁶

4. Experimental results

In this section we review a number of key experiments that teach us what resonance Raman spectroscopy can tell us about defects and disorder in sp^2 carbon materials.^{13–15,57}

4.1. *D*-Band in nanographites

The samples of nanographites used in the experiment were diamond-like carbon (DLC) films heat treated at different temperatures thus, giving rise to nanographites with different L_a values.¹³ The heat treatment was made using an electrical furnace setup, at T_{htt} of 1800, 2000, 2200, 2300, 2400, 2600 and 2700 °C. Before heat treatment, the sp^3 and sp^2 carbon phases coexist in the samples, but the sp^3 phases completely disappear for $T_{\text{htt}} > 1600$ °C.⁵⁸ Therefore, the samples used in this work correspond to aggregates of nanographite crystallites.

Fig. 7a shows STM images of the samples obtained at different T_{htt} . The evolution of the crystallite sizes with increasing T_{htt} is clearly observed from the STM images. The grain boundaries are very clear, and the samples show good structural homogeneity. A high resolution STM analysis shows that the *c* axis is always perpendicular to the sample surface.¹³ Fig. 7b shows the evolution of the (100) X-ray diffraction peak obtained using synchrotron radiation, for the samples heat treated at different T_{htt} . The crystallite size L_a was obtained by evaluating L_a from the Scherrer relation $L_a = 1.84\lambda/\beta\cos\theta$, where λ is the synchrotron radiation wavelength (0.120 nm), θ is the position of the (100) peak, and β is the half-height width of the (100) peak of graphite in $2\theta(\text{rad})$ units.¹³ The mean crystallite sizes obtained by X-ray diffraction are in good agreement with the L_a values obtained directly from the STM images ($L_a = 20, 35, 65, 150, 190, 340$,

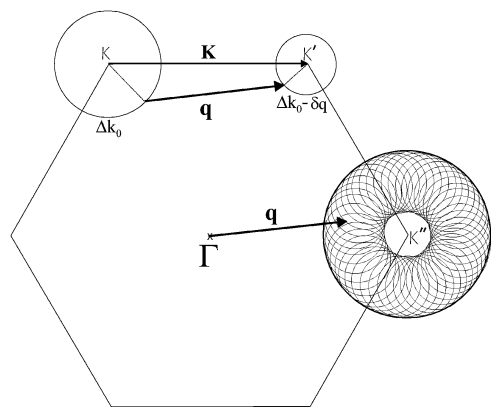


Fig. 6 In this inelastic scattering process, the initial (or final) \mathbf{k} and the intermediate $\mathbf{k} + \mathbf{q}$ states exist on equi-energy contours of the electronic structure. The possible \mathbf{q} states are on circles which we rotate around the *K* point.^{53,57} Here we neglect the trigonal warping effect.

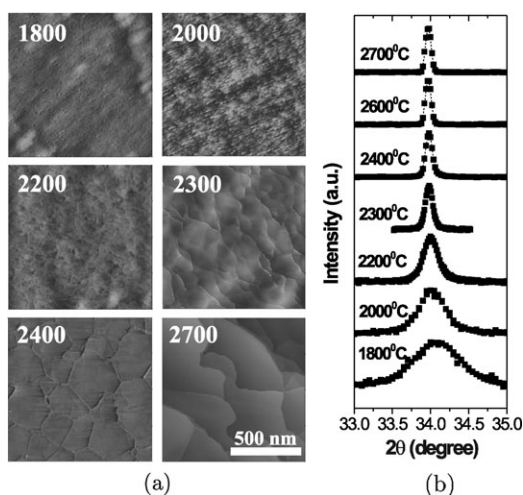


Fig. 7 (a) STM images of the sample heat treated at different temperatures. All images are shown in the same scale ($1 \mu\text{m} \times 1 \mu\text{m}$). (b) X-Ray diffraction profile of the (100) peak for samples heat treated at different temperatures.¹³

and 490 nm for the samples heat treated at $T_{\text{htt}} = 1800, 2000, 2200, 2300, 2400, 2600$, and $2700 \text{ }^{\circ}\text{C}$, respectively).¹³

Raman scattering experiments were performed at room temperature using a triple monochromator micro-Raman spectrometer (DILOR XY) for the following laser energies (wavelengths): krypton 1.92 eV (647 nm) and 2.18 eV (568 nm), and argon 2.41 eV (514.5 nm), 2.54 eV (488 nm) and 2.71 eV (457.9 nm). The laser power density was always less than 10^5 W cm^{-2} . Fig. 8a shows the Raman spectra of the D, G and D' bands for the $T_{\text{htt}} = 2000 \text{ }^{\circ}\text{C}$ sample for five different E_{laser} (1.92, 2.18, 2.41, 2.54, and 2.71 eV), noting that the ratio (I_D/I_G) is strongly dependent on E_{laser} . Therefore, it is clear that the empirical formula proposed by Knight and White⁴³ for the determination of L_a from the I_D/I_G ratio must be generalized for other E_{laser} values. Fig. 8b shows the Raman spectra using $E_{\text{laser}} = 1.92 \text{ eV}$ for samples with different T_{htt} values, giving rise to samples with different crystallite sizes L_a .

It is important to notice the small linewidths (γ_D) observed for the disorder-induced bands shown in Fig. 8, even for

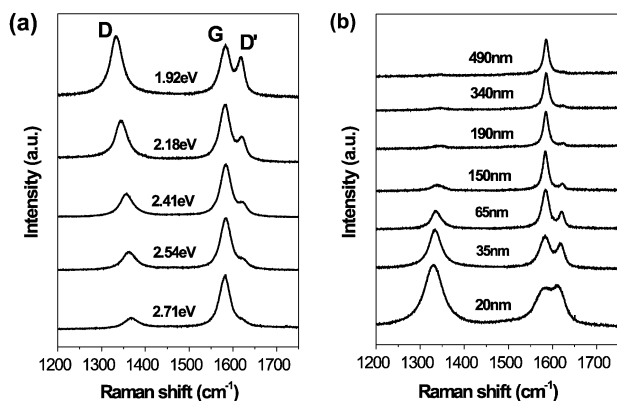


Fig. 8 The first order Raman spectra of (a) the sample heat treated at $2000 \text{ }^{\circ}\text{C}$, for five different laser energy values (1.92, 2.18, 2.41, 2.54, and 2.71 eV) (b) samples with different crystallite sizes using 1.92 eV laser excitation energy.¹³

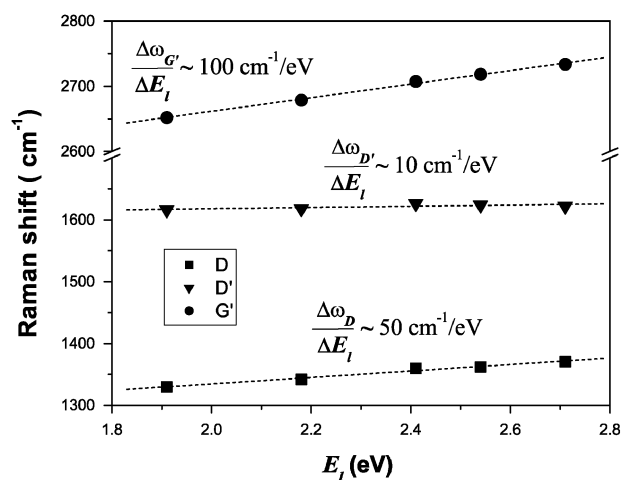


Fig. 9 Laser energy dependence of the frequency of the D, D' (Fig. 8) and G' bands.⁴⁶

samples with crystallite sizes as small as $L_a = 20 \text{ nm}$ (see linewidths for spectra at ref. 7 and 8 for comparison). These small γ_D are due to the well-defined boundaries of the crystallites and their narrow size distribution, as can be observed in the STM images in Fig. 7a. It was even possible to obtain STM images with atomic resolution on the surface of the samples heat treated up to $2200 \text{ }^{\circ}\text{C}$, indicating the high crystallinity degree of the crystallites.

Fig. 9 shows the laser energy dependence of the frequency of the D, D' and G' bands.⁴⁶ The slope associated with the G'-band is about $100 \text{ cm}^{-1}/\text{eV}$ and is two times the slope of the D-band ($50 \text{ cm}^{-1}/\text{eV}$). The D' band also exhibits a weak dispersive behavior, the slope being about $10 \text{ cm}^{-1}/\text{eV}$.

Fig. 10a shows a plot of (I_D/I_G) vs. $1/L_a$ for all samples and using five different E_{laser} values. Notice that I_D/I_G for a given sample is strongly dependent on E_{laser} . However, as illustrated in Fig. 10b, all curves shown in part (a) collapse on to the same curve in the (I_D/I_G) E_{laser}^4 versus $1/L_a$ plot. This result shows that, for the nanographite sample shown in Fig. 8, the ratio I_D/I_G is inversely proportional to the fourth power of E_{laser} , and a general equation for the determination of the crystallite size L_a using any laser line in the visible range can be written as:¹³

$$L_a(\text{nm}) = \frac{560}{E_{\text{laser}}^4} \left(\frac{I_D}{I_G} \right)^{-1}, \quad (1)$$

where E_{laser} is the excitation laser energy in eV used in the Raman experiment. Considering the laser line wavelength (λ_{laser}) in nm units, eqn (1) can be rewritten as:

$$L_a(\text{nm}) = (2.4 \times 10^{-10}) \lambda_{\text{laser}}^4 \left(\frac{I_D}{I_G} \right)^{-1}. \quad (2)$$

These systematic studies will be useful for the characterization of the next generation of graphene samples with one, two and more layers in evaluating L_a and in exploring the boundary scattering defects in their samples.

4.2. The D-band from edge defects

The edges of a nanographite sample also can be considered as defects and can contribute to the D-band spectra. Of

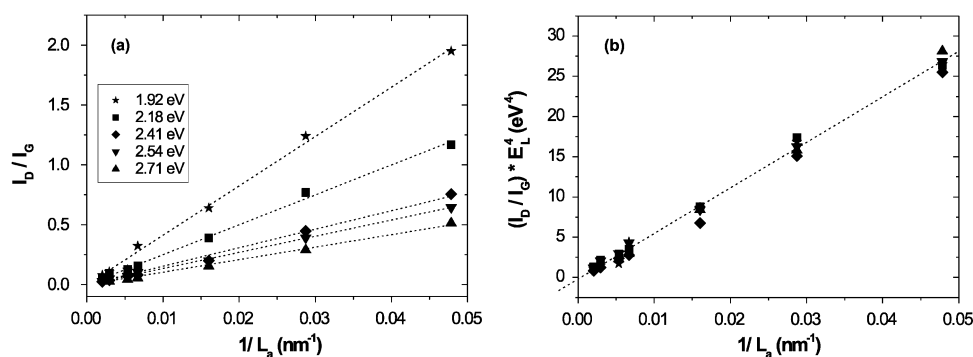


Fig. 10 (a) The intensity ratio I_D/I_G versus $1/L_a$ using five different laser excitation energies is plotted. (b) All curves shown in part (a) collapse on the same curve in the $(I_D/I_G)E_L^4$ versus $1/L_a$ plot where $E_L = E_{\text{laser}}$.¹³

particular interest is the study of the contrasting Raman spectra obtained from an armchair edge and from a zigzag edge of a nanographite sample.

Fig. 11 shows three back-scattering Raman spectra obtained at different regions of a highly oriented pyrolytic graphite (HOPG) sample. The inset to Fig. 11 shows an optical image of the sample. Regions 1 and 2 are at HOPG edges, while region 3 is on the flat HOPG surface. Spectra were obtained with the incident light polarization parallel to the respective edge direction. The G band, centered at 1580 cm⁻¹ is present in all spectra with the same intensity. The disorder-induced D and D' bands are observed in spectra 1 and 2, but not in spectrum 3. This result shows that the edge behaves as a defect necessary for momentum conservation in the double resonance Raman process. However, the most striking result shown in Fig. 11 is the fact that the D band is about four times less intense in spectrum 2 as compared to spectrum 1, whereas the D' band intensity remains almost constant in both spectra. The different intensities observed for the D band in spectra 1 and 2 indicate an intrinsic structural property of the scattering process for graphite edges.

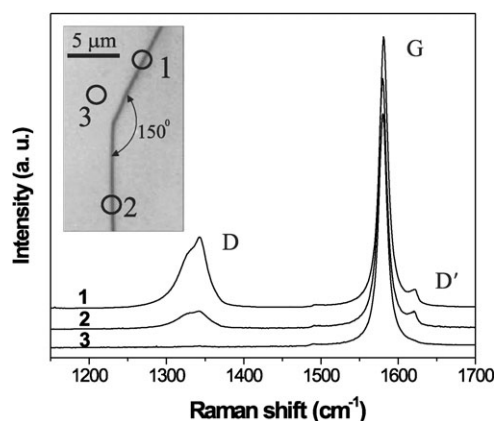


Fig. 11 Raman spectra obtained in three different regions of the HOPG sample. The spectra were taken at room temperature. The laser power density on the sample was 3×10^5 W cm⁻² and the laser energy was 1.96 eV. The inset shows an optical image of the step and the regions where spectra 1, 2, and 3 were taken (open circles). Spectra 1 and 2 were obtained with the incident light polarization parallel to the respective edge direction.¹⁵

To structurally characterize the sample, scanning probe microscopy measurements were performed. Fig. 12a shows an AFM image of the step on the HOPG substrate where the Raman measurements in Fig. 11 were performed. The step height is about 230 nm. Fig. 12b shows another AFM image of the edge 2 and scanning tunneling microscopy (STM) measurements were performed in the region marked by the white X in Fig. 12b. The raw STM data (Fig. 12c) exhibit atomic spacing resolution, allowing a structural analysis of the edges to be made: Fig. 12d shows an FFT-filtered zoom image of the region marked by a white square in Fig. 12c. There are two inequivalent atoms in the graphite unit cell, A and B, and STM measurements performed in the basal plane of graphite are normally able to distinguish one of them (B atoms),⁵⁹ which corresponds to the dark regions in Fig. 12d. The positions of the A atoms are also indicated by small black squares in Fig. 12d. A zigzag line connects A and B neighbor atoms and, following the white dashed line in Fig. 12b, c and d, it can be concluded that edge 2 has a zigzag structure. Therefore, edge 1 must have an armchair structure since, as shown in Fig. 11 and 12a, edges 1 and 2 form an angle of 150° with respect to each other [see Fig. 12a].

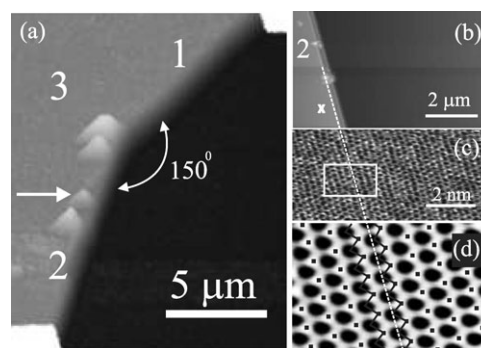


Fig. 12 (a) AFM image of the step on the HOPG substrate where the Raman spectra shown in Fig. 1 were taken. (b) AFM image of edge 2. (c) Atomic resolution STM image of the region marked by the white X in part (b). The STM measurements were performed under ambient conditions in the constant-height mode. (d) Fast Fourier transform (FFT) filtered image from the region marked by a white square in part (c). Edge 1 is an armchair edge which gives a strong D-band intensity.¹⁵

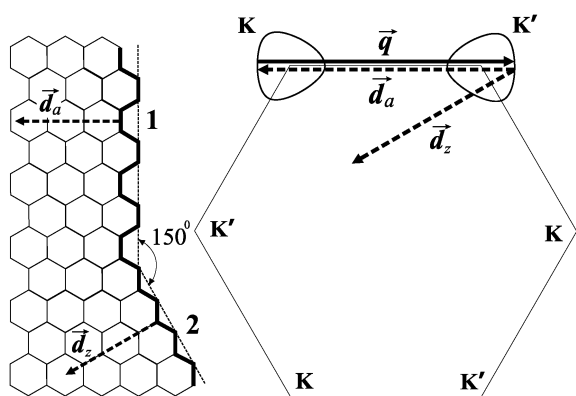


Fig. 13 Schematic illustration of the atomic structure of the armchair and zig-zag edges and first BZ of 2-D graphite, showing the double resonance mechanism for an armchair graphite edge. In contrast to Fig. 6, here the trigonal warping has been considered.

The most common case of disorder-induced bands in the Raman spectra of graphite-related materials occurs in samples formed by aggregates of small crystallites. In this case, the crystallite borders (grain boundaries) form defects in the real space. Since the crystallites have different sizes and their boundaries are randomly oriented, the defect wavevectors exhibit all possible directions and values. Therefore, the existence of a defect with momentum exactly opposite to the phonon momentum is always possible, giving rise to double resonance processes. However, in the case of edges, the *D* band intensity is anisotropic because the double resonance process cannot always occur for any arbitrary pair of points. Since, the edge defect in real space is well localized in the direction perpendicular to the edge, it is completely delocalized in this direction in reciprocal space and, therefore, the wavevector of such a defect assumes all possible values perpendicular to the step edge. Hence, the defect associated with a step edge has a 1D character and it is only able to transfer momentum in the direction perpendicular to the edge.

Fig. 13 shows the structure of the two kinds of edges shown in Fig. 11 and the first BZ of 2-D graphite oriented according to the real space lattice. The bold lines show the edge structures, armchair for edge 1 and zigzag for edge 2. The wavevectors of the defects associated with these edges are represented by \vec{d}_a for armchair and \vec{d}_z for the zigzag edge. Note that only the armchair \vec{d}_a vector is able to connect points belonging to equi-energy contours centered at two inequivalent *K* and *K'* points in Fig. 13. The size of the equi-energy contours around the *K'* and *K* points are not large enough to allow the connection of any \vec{k}' and \vec{k} states by a zigzag \vec{d}_z vector in a Raman experiment performed with visible light.⁵⁷ Therefore, the inter-valley double resonance process associated with this defect cannot occur for a perfect zigzag edge.

The mechanism depicted in Fig. 13 can thus explain the results shown in Fig. 11. The *D* band is much less intense in the spectra obtained in edge 2, which has a zigzag structure. On the other hand, the *D'* band, around 1620 cm⁻¹, arises from an intra-valley process, which connects points belonging to the same equi-energy contour around the *K* (or *K'*) point. In this case, momentum conservation can be satisfied by both \vec{d}_a and

\vec{d}_z vectors and, therefore, the observation of the *D'* band must be independent of the edge structure. This conclusion is confirmed by the experimental result shown in Fig. 11, where the *D'* band has the same intensity in both spectra 1 and 2, with armchair and zigzag structures, respectively.

These edges (see Fig. 11) can be distinguished spectroscopically by measuring the intensity of a disorder-induced Raman *D*-band.¹⁵ The *D*-band appears as a consequence of a double resonance (DR) Raman process^{53–55} which involves the scattering of the electron by one phonon and one defect (see section 3 and section 4.4). In order to have momentum conservation, the momenta of the phonon and the defect must have approximately the same value but with opposite directions. The 1-D defect, perpendicular to the edge, selects the direction of the electron and phonon associated with the disorder-induced Raman process, and causes a dependence of the Raman *D* band intensity on the atomic structure of the edge (strong for armchair and weak for the zigzag edge). The influence of the defect structure on the Raman spectra of graphite-like systems may be very useful to characterize defects in nanographite-based devices, such as nanographene sheets² that present a great potential for both basic physics and application in nanoelectronics.

4.3. Stokes and anti-Stokes spectra of the *D*-band and *G'*-band

The study of the Stokes and anti-Stokes spectra for the *D* and *G'* bands is important for a deep exploration of the complexity of the double resonance process in graphite related materials. This rich phenomenon is responsible, for example, for the Raman based signature of 2-D vs. 3-D graphite systems. Fig. 14 shows the Stokes and anti-Stokes spectra of the *D*-band and *G'*-band for disordered turbostratic graphite for which there is no stacking order between adjacent graphene planes. In order to compare these two spectral features, the *D*-band is plotted on a doubly expanded horizontal axis. An interesting experimental result observed in Fig. 14 concerning the *D* band is the fact that its position is not exactly the same in the Stokes (S) and anti-Stokes (AS) spectra (ω_D is smaller in the Stokes spectrum).^{57,60} Moreover, the frequency of the overtone *G'*-band is not twice the *D*-band frequency, with $\omega_{G'}$ being smaller than $2\omega_D$ in the S spectrum and greater than $2\omega_D$ in the AS spectrum.^{57,60}

The left part of Fig. 15 shows the four possible double resonance (DR) mechanisms associated with the *D* band in the Stokes process. For the first process, depicted in the upper part of Fig. 15 [process (a)], an electron with momentum near the *K* point is resonantly excited from the π to the π^* band by an incident photon. The electron is then inelastically scattered, by the emission of a phonon with momentum $\hbar\mathbf{q}$, to a point near the *K'* point in the π^* band. This is a resonant process since it connects two real electronic states. The electron is scattered back by a defect, and in this case the back-scattering is elastic and non-resonant. Finally the electron-hole recombination gives rise to a scattered photon with energy $E_{\text{laser}} - E_{\text{phonon}}$, which is not resonant with the $\pi^* - \pi$ transition.

In the second process depicted in Fig. 15 [process (b)], the scattering from a point around *K* to a point around *K'* is elastic and occurs *before* the inelastic back-scattering,

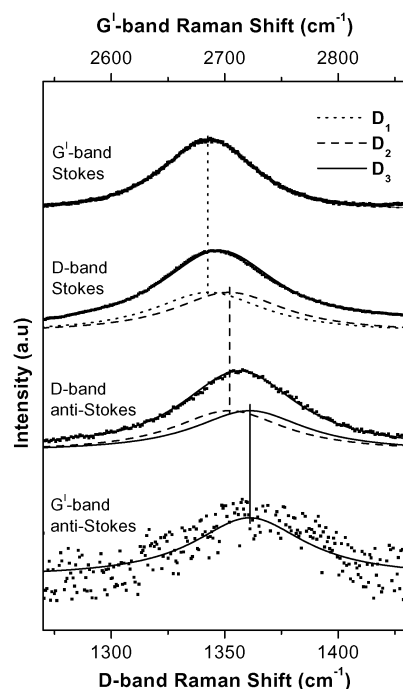


Fig. 14 Stokes and anti-Stokes spectra of the *D*-band and *G'*-band for disordered turbostratic graphite. In order to compare the *D*-band and *G'*-band spectra, the *D*-band spectra are plotted on a doubly expanded horizontal axis. Three Lorentzian functions D_1 , D_2 , D_3 , are used for fitting the Stokes and anti-Stokes *D*-band spectra in which D_1 is common with the Stokes *G'*-band, D_3 is common with the anti-Stokes *G'*-band, and D_2 is common with both the Stokes and anti-Stokes *D*-band spectra.^{53,57}

associated with the emission of the phonon. In processes (c) and (d) in Fig. 15, the incident photon is not in resonance with the π – π^* transition, and the resonance occurs only for the scattered photon in the electron-hole recombination. In this case, the electron-hole pair must have a different momentum compared to processes (a) and (b). In process (c), the inelastic scattering of the electron occurs before the elastic back-

scattering, whereas in process (d) the elastic scattering occurs before the inelastic scattering process.

There are also four possible mechanisms associated with the anti-Stokes scattering, represented by processes (a), (b), (c) and (d) in the right part of Fig. 15, which are equivalent to the Stokes processes (a), (b), (c) and (d), in the left part of Fig. 15, respectively. The only difference in this case is that the inelastic scattering, connecting points around the K and K' points, is due to the *absorption* of a phonon with wavevector q . Therefore, there is an increase of $E_{\text{phonon}} = \hbar\omega_q$ in the energy of the electron in the inelastic scattering process.

The double resonance processes associated with the *D*-band connect points in the circles around K and K' , as shown in Fig. 6. Process (a) in Fig. 15 connects points on the circles around K and K' with different radii.⁵⁷ Process (b) in Fig. 15 connects points along the two circles with the same radii around K and K' . For processes (c) and (d) in Fig. 15, the resonance occurs for the scattered photon. The radii of all circles around K and K' for all possible processes are also given in Fig. 15.

The double resonance mechanism is satisfied by any phonon whose wavevector connects two points in the circles around K and K' . Fig. 6 shows one of the possible DR mechanisms [process (a) in Fig. 15]. If the vector q is measured from the Γ (center) point in the BZ, its end is close to the K'' point in Fig. 6, which is equivalent to the K point by symmetry. As shown in Fig. 6, the set of all possible phonon q vectors connecting any points in the circles around K and K' , measured from the Γ point, have ends in the area between the two circles around K'' . The radii of the inner and outer circles around K'' correspond to the modulus of the difference and the sum of the radii of the two circles around K and K' .

There is a high density of phonon wavevectors q satisfying the DR mechanism for which the end of the wavevectors measured from the Γ point are in the inner and outer circles around K'' . The phonons associated with the singularities in the density of q vectors are expected to make a significant contribution to the DR Raman spectra. Notice that the radius of the inner circle around K'' does not depend on the laser energy. However, the associated DR phonon singularity

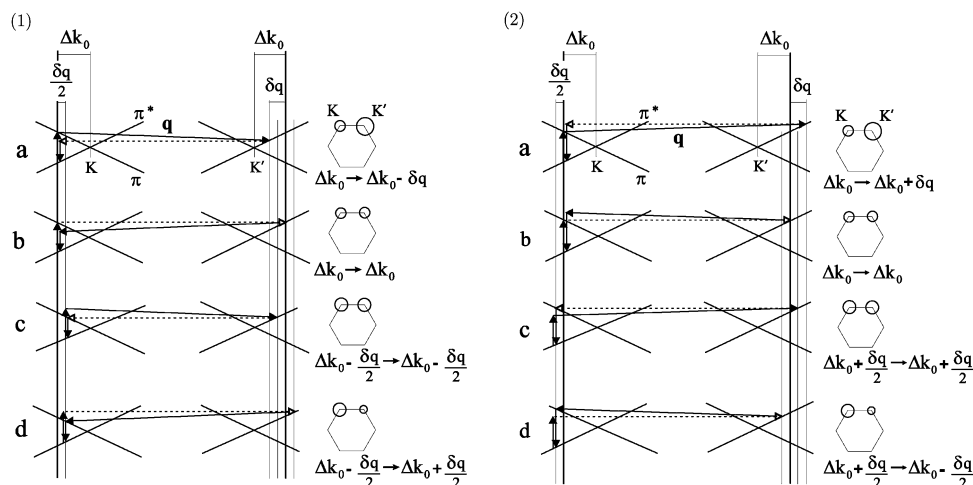


Fig. 15 Intervalley, double resonance scattering processes for (1) Stokes and (2) anti-Stokes processes.^{53,57}

doesn't give rise to a Raman band since the electron–phonon coupling is very small in this case.

The singularity associated with the outer circle gives rise to the *D*-band. Considering all possible S and AS processes, we conclude that the *D*-band is composed of two peaks D_1 and D_2 in the S spectrum, and two peaks D_2 and D_3 for the AS spectrum. The D_2 peak is expected to appear in both the S and AS spectra. The double resonance mechanism of the second-order G' -band involves two phonons, instead of one phonon and one defect. In this case, only processes (a) and (c) in Fig. 15 are possible, since the resonant scattering from a circle around K to a circle around K' is always associated with the emission (or absorption) of a phonon. Therefore, we must expect a single peak for the G' -band, centered at $2\omega_{D1}$ and $2\omega_{D3}$ in the Stokes and anti-Stokes spectra, respectively.

It is interesting to observe that the D_1 peak is associated with processes (a) and (c) in Fig. 15, whereas D_2 is associated with processes (b) and (d). Therefore, we conclude that the two peaks in the S and AS *D*-band are not related to resonances with the incident and scattered photons, but rather are associated with the scattering from a point around K to a point around K' , by a phonon [processes (a) and (c)] or by a defect [processes (b) and (d)].⁵⁷ Thus, the *D*-band (one-phonon DR) can be fit by two Lorentzians, while the G' -band (two-phonon DR) is fit by just one Lorentzian,⁵⁷ since no defect scattering event is needed in this case (see Fig. 5c1 and c2). Finally, this rich phenomenon is responsible for the different Raman spectra between 2-D and 3-D graphite, and can be used even for differentiating between one, two or a few graphene layers in a sample, as discussed below.

4.4. Measuring stacking order by Raman spectroscopy

In the next wave of two or more layer graphene sample preparation, samples will likely be prepared with some turbostratic stacking, in contrast with the early samples used in the graphene studies that were based on HOPG.^{16–18} Whereas HOPG has very few AB stacking faults, it is likely that the next generation of samples containing larger areas of graphene layer stacks will have more stacking faults or will even lack interlayer AB alignment. To characterize such samples for their appropriateness for specific studies of the electronic, phonon or magnetic properties, systematic Raman characterization will be needed to evaluate bilayer and multilayer graphene samples for their AB stacking faults. STM measurements that distinguish between 3-fold and 6-fold symmetry provides an alternate method for evaluating the amount of stacking faults in graphite or bilayer and multilayer graphene samples.⁶¹ For the stacking order structure, there are two limits that are of particular importance. One is the difference between one and two graphene layers, and the other is the evolution from turbostratic (2-D) to highly oriented pyrolytic (3-D) graphite. When moving from one to two graphene layers, the unit cell change from a two atom to a four atom unit cell. This generates a splitting of almost all the electronic and phonon bands. The splitting of the electronic bands is measurable, thus leading to a change in the G' band from a one to four peak structure,^{16–18} as pointed out in the previous section.

In a turbostratic graphite there is no stacking order between adjacent layers and the interlayer separation (>0.342 nm) is larger than that for crystalline graphite (0.335 nm). The absence of stacking order between the graphene planes results in a very weak interaction between adjacent planes so that turbostratic graphite can be considered to be 2-D graphite to a first approximation. The very recent development of experimental methods which allow the formation of graphite samples with a small and controlled number of graphene sheets (1, 2 or more), has increased the capability of Raman spectroscopy to characterize interesting graphitic materials and to distinguish between such materials from one another. It was shown by different groups^{16–17} that the shape of the G' -band is strongly dependent on the number of graphene layers in the sample, thus showing that it is possible to differentiate by Raman spectroscopy the number of graphene layers in a sample with a small number of sheets (1, 2 or more). The G' -band for just one graphene sheet is composed of a single Lorentzian peak with FWHM = 30 cm^{-1} but four Lorentzian peaks are needed to fit the G' -band for a sample with two graphene layers with AB interlayer stacking.^{16,17} With an increasing number of graphene layers, the shape of the G' -band tends to that of a 3-D graphite, for which the lineshape can be fit by two Lorentzian peaks.^{16,17} The systematic study of AB stacking disorder relates to defects expected to occur in graphene samples that are now being prepared for scientific studies and potential practical applications.

Fig. 16 shows the G' band spectra obtained using the 514.5 nm wavelength 2.41 eV laser excitation from disordered sp^2 carbon films with thicknesses of several microns, heat treated at different T_{ht} . The Raman spectrum of the sample heat treated at 2200 °C (bottom part) can be fit using only one single peak centered at 2707 cm^{-1} , called here G'_{2D} . This is the typical profile of the G' band in Raman spectra of turbostratic graphite samples, where there is no stacking order along the c axis. The FWHM of this band is about 42 cm^{-1} , which is just a

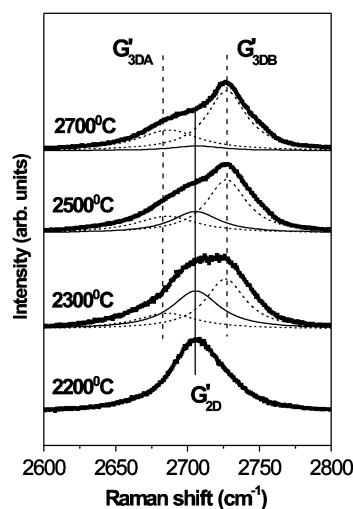


Fig. 16 G' band Raman spectra of samples heat treated to various temperatures T_{ht} , performed using $E_{\text{laser}} = 2.41\text{ eV}$ (514.5 nm). The G' band changes from one peak to two peaks with increasing T_{ht} .¹⁴

little larger than the FWHM of a single graphene layer (30 cm^{-1}).^{16,17} The similarity of the Raman G' -band spectrum of a turbostratic graphite to that of a single graphene sheet provides direct experimental evidence that a turbostratic graphite can be considered as a 2-D graphite.

At the top of Fig. 16, the spectrum of the sample heat treated at 2700°C shows a two peaks shape, which is a typical profile for the G' band in 3-D graphite. Notice that this G' band can be fit using two Lorentzians (G'_{3DA} and G'_{3DB}) centered at 2687 cm^{-1} and 2727 cm^{-1} , respectively. The Raman spectra of the samples heat treated at intermediate temperature values (2300°C , and 2500°C) show the evolution from one single peak to two peaks. Three Lorentzian peaks are needed to fit the Raman spectra of these samples, which are in the intermediate situation between 2-D and 3-D graphite. The relative intensity (integrated area) of the G'_{3DA} and G'_{3DB} peaks ($I_{G'_{3DA}}$ and $I_{G'_{3DB}}$, respectively) increases while the relative intensity of the G'_{2D} peak ($I_{G'_{2D}}$) decreases with increasing heat treatment temperature. Furthermore, for all spectra depicted in Fig. 16, the intensity ratio of the peaks G'_{3DA} and G'_{3DB} is constant, being $I_{G'_{3DB}}/I_{G'_{3DA}} \sim 2$. The changes in the G' band shape, from one peak (one graphene layer) to two peaks (many graphene layers) reveals different degrees of stacking order along the c direction.

This one vs. two peak lineshape in the G' feature has been used recently to understand the structure of the recently developed pitch-based graphitic foams.²⁰ Raman spectroscopy studies were performed on the different regions of the graphitic foam, yielding important information on the structural properties of the graphitic foams, as well as on the physical properties of graphite. The graphitic foam was found to be composed of two intermixed graphitic structures, one with stacked planes and one with a turbostratic structure. This special structure allowed for a simultaneous study of the properties of 2-D and 3-D graphitic structures. The dispersion $\Delta\omega_{G'}/\Delta E_{\text{laser}}$ of the G' -band was found to be different for 2-D and 3-D graphite. The intensity of the D -band Raman feature was used to probe the density of defects in the structure, leading to the conclusion that the structural defects are mainly localized at the 2-D structures.²⁰

5. Theoretical results

5.1. Raman intensity formula

The Raman intensity $I(\omega, E_{\text{laser}})$ of the D -band, which is due to a double resonance scattering process, is given by:⁵

$$I(\omega, E_{\text{laser}}) = \sum_j \left| \sum_{a,b,c,\omega_{\text{ph}}} \frac{M_{\text{op}}(\mathbf{k}, jc) M_{\text{elastic}}(-\mathbf{q}, cb) M_{\text{ep}}(\mathbf{q}, ba) M_{\text{op}}(\mathbf{k}, aj)}{\Delta E_{aj}(\Delta E_{bj} - \hbar\omega_{\text{ph}})(\Delta E_{aj} - \hbar\omega_{\text{ph}})} \right|^2, \quad (3)$$

where $\Delta E_{aj} = E_{\text{laser}} - (E_a - E_j) - i\gamma$, and γ denotes the broadening factor, taken to be $\gamma = 0.06 \text{ eV}$.⁵ Here j, a, b and c denote the initial state, the excited state, the first scattered state of an electron by a phonon and the second scattered state of an electron by a defect, respectively. M_{op} , M_{ep} and M_{elastic} denote the electron–photon, electron–phonon and elastic scattering matrix elements, respectively. As we see in Fig. 5, the process

for which elastic scattering occurs first is also possible. For a given initial and final state, all intermediate states are added before taking the square. Thus in some cases, the two processes interfere with each other to give either an enhanced or reduced intensity.^{62,63}

5.2. Elastic scattering

The elastic electron scattering at the armchair edges from electron state k to k' is expressed by the matrix element

$$M_{\mathbf{k}'\mathbf{k}} = \langle \Psi^c(\mathbf{k}') | V | \Psi^c(\mathbf{k}) \rangle, \quad (4)$$

in which $\Psi^c(\mathbf{k})$ is the conduction-band wavefunction of two-dimensional (2-D) graphite at wavevector \mathbf{k} and V is the potential term of the Hamiltonian. $\Psi(\mathbf{k})$ is expanded by the Bloch wavefunction Φ_s ,

$$\Psi^c(\mathbf{k}, \mathbf{r}) = \sum_{s=A,B} C_s^c(\mathbf{k}) \Phi_s(\mathbf{k}, \mathbf{r}), \quad (5)$$

and Φ_s is expressed by the atomic wavefunction, $\phi(\mathbf{R}-\mathbf{R}_s)$:

$$\Phi_s(\mathbf{k}, \mathbf{r}) = \frac{1}{\sqrt{N_u}} \sum_{\mathbf{R}_s} e^{i\mathbf{k}\mathbf{R}_s} \phi(\mathbf{r} - \mathbf{R}_s), \quad (6)$$

in which N_u , $C(\mathbf{k})$, \mathbf{R}_s are, respectively, the number of graphite unit cells in the crystal, the wave function coefficient and the coordinate of the A or B atom of the s -th unit cell in the crystal and appearing in the atomic orbital. In the absence of a defect, $\Phi(k)$ is an eigenfunction of 2-D graphite. When we substitute eqn (5) into eqn (4), we get

$$M_{\mathbf{k}'\mathbf{k}} = \frac{1}{N_u} \sum_{s,s'} C_{s'}^*(\mathbf{k}') C_s(\mathbf{k}) \sum_{\mathbf{R}_s, \mathbf{R}_{s'}} \times \exp(-i\mathbf{k}'\mathbf{R}_{s'} + i\mathbf{k}\mathbf{R}_s) \langle \phi(\mathbf{R}_{s'}) | V | \phi(\mathbf{R}_s) \rangle. \quad (7)$$

Here we consider only interactions between nearest-neighbor carbon atom sites:

$$\langle \phi(\mathbf{R}_s) | V | \phi(\mathbf{R}_{s'}) \rangle = \begin{cases} \gamma_0 & s, s' (\text{nearest neighbor}) \\ 0 & \text{otherwise} \end{cases} \quad (8)$$

For a k vector around the K point, we have two possibilities, that is, an intravalley or intervalley scattering process. The D -band corresponds to intervalley scattering. Here we only consider the scattering at the armchair edge as is discussed in Fig. 13.^{6,15} After some calculation,⁶⁴ the intervalley matrix elements $M_{\mathbf{k}'\mathbf{k}}$ are given by

$$M_{\mathbf{k}'\mathbf{k}} = -\frac{a\gamma_0}{2L_a w(\mathbf{k})} \delta(k_x, k'_x) \left[2w^2(\mathbf{k}) \cos\left\{ \frac{(k'_y - k_y)L_a}{2} \right\} - \left\{ \exp\left(-i\frac{\sqrt{3}k_x a}{2} \right) + 2\cos\left(\frac{k_y a}{2} \right) \right\} \cos\left\{ \frac{k_y a}{2} - \frac{(k'_y - k_y)L_a}{2} \right\} - \left\{ \exp\left(i\frac{\sqrt{3}k'_x a}{2} \right) + 2\cos\left(\frac{k'_y a}{2} \right) \right\} \cos\left\{ \frac{k'_y a}{2} + \frac{(k'_y - k_y)L_a}{2} \right\} \right], \quad (9)$$

where $\delta(k_x, k_x')$ is a delta-function due to momentum conservation, and $f(\mathbf{k})$ and $w(\mathbf{k})$ are given by³

$$f(\mathbf{k}) = \sum_{i=1}^3 f_i(\mathbf{k}) = \sum_{i=1}^3 e^{ik \cdot \mathbf{b}_i}, \quad (10)$$

$$w(\mathbf{k}) = \sqrt{|f(\mathbf{k})|^2}. \quad (11)$$

The momentum conservation $k_x = k_x'$ in eqn (9) for an armchair edge is also valid at a zigzag edge, as discussed in section 4.2 and ref. 15. This momentum conservation indicates that the allowed elastic scattering \mathbf{q} vector must be perpendicular to the k_x axis. In the case of the zigzag edge, the intervalley scattering \mathbf{q} vector should connect K to K' (or K' to K).⁶ Thus, intervalley scattering can not occur at the zigzag edge. On the other hand, at the armchair edge, both intravalley and intervalley scattering can occur,¹⁵ as shown in Fig. 13.

The scattering of an electron at the edge may modify the electronic structure around the edge. This effect is understood by considering multi-scattering processes or the T-matrix for a scattering problem.^{65,66} Eqn (4) is the first approximation to the scattering process. The application of the T-matrix for the elastic scattering matrix element remains for future work.

The theoretical developments in this section can now be applied to calculating Raman spectral features associated with double resonance processes.

5.3. Optical matrix elements and electron–phonon matrix elements

The other matrix elements that are needed for the Raman spectra calculation such as optical matrix elements for absorption and emission, and electron–phonon interaction, are the same ones that were used to calculate the Raman intensity for the first-order Raman spectra.⁶² For the case of 2-D and 3-D graphite, sigma bonds can be ignored, and we then only consider the electron–phonon interaction for π -electrons.⁶² For calculating the lattice vibration amplitude, the number of phonons for the various energies can be calculated by using the Bose–Einstein distribution function for phonon emission and absorption ($\beta = 1/k_B T$) with $T = 300$ K for room temperature spectra.

The electronic structure calculation is based on the extended tight binding (ETB) method⁶⁷ and the phonon energy dispersion is calculated by a molecular dynamics calculation in which we adopt Dubay's force constants⁶⁸ up to the twentieth nearest neighbors. The calculated phonon dispersion curves (Fig. 1a) thus obtained reproduce well the phonon dispersion curves for graphite obtained by inelastic X-ray measurements.²³ Further we assume that the iTO phonon branch around the K point is approximated by the linear function⁶⁴ $\hbar\omega_q = 1250\hbar + 973q$ cm^{−1} which is discussed in terms of Kohn-anomalies by Piscanec *et al.*²⁶ This approximation for the experimental results is important to reproduce the width and the dispersion of the observed spectral features of the D -band in graphite.

5.4. Calculated results

To calculate the dependence of the D -band intensity on the crystallite size L_a , a nanographite ribbon with width L_a (see

Fig. 2) is considered and the D -band intensity is explicitly calculated for a nanographite ribbon with an armchair edge.¹⁵ The nanographite ribbon has a one-dimensional (1-D) structure with an armchair edge at $y = \pm L_a/2$ and a zigzag edge at $x = \pm L_a/2$ as shown in Fig. 2. In a nanographite ribbon, we have both zigzag and armchair edges,³³ but the zigzag edge does not contribute to the elastic scattering from the K to K' points in the BZ, as shown in Fig. 13. Therefore a simple model with the armchair edge is used in which the elastic scattering at the edge is expressed by the width of the nanographite ribbon L_a . In a real disordered graphite sample, we expect defects, other than edge defects, such as vacancy, dopant, impurity, strain *etc.* The present model is, however, useful for getting an analytic expression for the elastic scattering.

In Fig. 17 we show the calculated spectral D -band Raman intensity for the three different laser energies of 1.90 eV (solid), 2.30 eV (dashed) and 2.70 eV (dotted lines).⁶⁴ The D -band peaks in the 1350–1400 cm^{−1} range come from the iTO phonon dispersion branch which has A_1 symmetry at the K point. The slope of the D -band frequency *vs.* E_{laser} from the results of Fig. 17 is $\Delta\omega_D/\Delta E_{\text{laser}} = 50$ cm^{−1}/eV, which reproduces the experimental value⁶⁹ very well (see inset of Fig. 17). Note that the calculated D -band feature in Fig. 17 is asymmetric, in contrast with the symmetric shape of the experimentally observed D -band (see Fig. 8). Further theoretical work is needed to explain the observed shape of the D -band.

Fig. 18 shows the calculated⁶⁴ dependence of the I_D/I_G ratio on (a) E_{laser} and (b) L_a (dashed lines). Here we are neglecting the I_G dependence on either E_{laser} or L_a (I_G is selected to be a constant, fitted to the I_D/I_G value for $L_a = 57$ nm and $E_{\text{laser}} = 2.41$ eV). Square points in Fig. 18 denote the experimental data¹³ shown for comparison. The results of Fig. 18 show that the E_{laser} dependence of I_D/I_G is in good agreement with the experimental results, while the L_a dependence shows a discrepancy between experiment and theory, the experimental

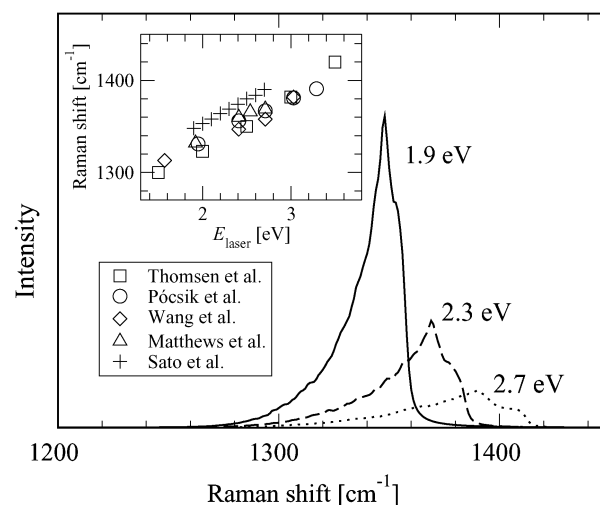


Fig. 17 The calculated Raman spectra of the D -band for $E_{\text{laser}} = 1.90$ eV (solid line), 2.30 eV (dashed line), 2.70 eV (dotted line).⁶⁴ The inset shows a comparison of ω_D *vs.* E_{laser} between various works.^{49,51,64,69,70}

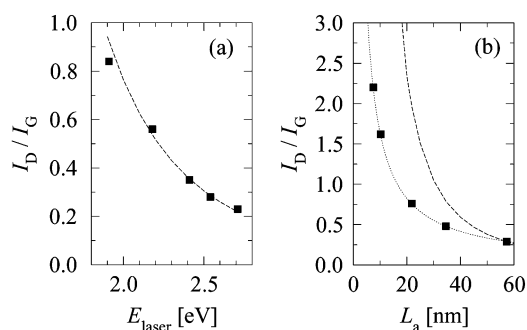


Fig. 18 (a) The laser energy dependence of I_D/I_G at $L_a = 57$ nm. (b) The crystallite size dependence of I_D/I_G at $E_{\text{laser}} = 2.41$ eV. The square points and dashed lines are, respectively, experimental and calculated results. The dotted line in (b) is a calculated result with additional dependence of γ on L_a (see text in section 5.4).

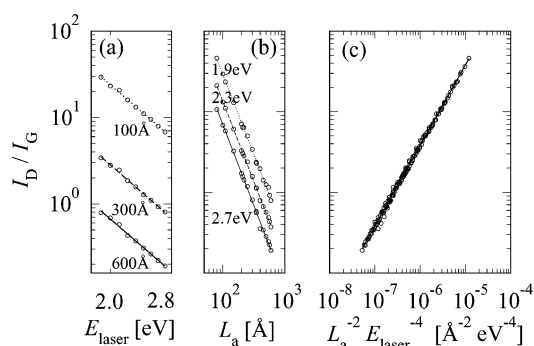


Fig. 19 Log-log plots of the calculated dependence of the ratio I_D/I_G on: (a) E_{laser} , (b) the crystallite size L_a , and (c) the product $L_a^{-2} E_{\text{laser}}^{-4}$ to give a universal curve. Open circles denote calculated values.

results being proportional to L_a^{-1} , while the calculated results give I_D/I_G proportional to L_a^{-2} . In order to see this dependence, we show in Fig. 19 a log-log plot of the calculated results of the I_D/I_G ratio dependence on: (a) E_{laser} and (b) L_a and (c) $L_a^{-2} E_{\text{laser}}^{-4}$. The reason for $I_D/I_G \propto L_a^{-1}$ in the calculations is due to the normalization factor L_a^{-2} in eqn (9). The weak L_a dependence in the experiments might come from: (1) another origin of defects or (2) an L_a dependence on the resonance width γ which will be clarified in future experiments. In fact, when we take $\gamma \sim C/\sqrt{L_a}$ (where C is a constant), then we can reproduce the experimental results (dotted line in Fig. 18b) for the case of an elastic scattering process. The justification for $\gamma \sim C/\sqrt{L_a}$ comes from the fact that (1) carriers move diffusively so that $L_a \sim Dt_d^2$, where D is the diffusion constant and t_d is the diffusion time, and (2) from these results we can write $\gamma \sim \hbar/t \sim \sqrt{D}/\sqrt{L_a}$.

6. Conclusions and outlook for defect characterization in graphene and nanographite by Raman spectroscopy

In summary, we have presented an overview of the Raman spectra associated with defects in sp^2 graphitic materials from both experimental and theoretical standpoints. The disorder-induced D and D' Raman features, as well as the G' -band (the overtone of the D -band which is always observed in defect-free

samples), are discussed in terms of the double-resonance (DR) Raman process, involving both phonons within the interior of the 1st Brillouin zone of graphite and defects. Recent advances that made possible the development of a general empirical formula for the determination of in-plane crystalline sizes using any excitation laser energy are discussed. Results of the disorder-induced bands on both armchair and zig-zag edges show that the intensity of the D -band is higher at the armchair edges, showing that Raman spectra can provide information about the atomic structure at graphite edges. We briefly discuss recent Raman studies in graphene samples with one or a few layers, showing that Raman spectra can also be used to distinguish between single and multi-graphene layers.

Regarding theory, the D -band intensity has been studied systematically for nanographite materials with different laser excitation energies and crystalline sizes. Using the elastic scattering matrix element that is developed for armchair edges, the excitation energy dependence of the D -band intensity is reproduced by the double resonance Raman scattering approach. On the other hand, there is a discrepancy between theory and experiment regarding the L_a dependence of the Raman intensity. We further need to investigate the origin of the L_a dependence of I_D/I_G from both an experimental and theoretical standpoint.

Systematic studies of the disorder-induced Raman spectra for different types of defects and for different numbers of graphene layers is important to provide a framework for the possible future use of Raman spectroscopy to distinguish one type of defect from another. Near field Raman spectroscopy, with higher spatial resolution than micro Raman spectroscopy, must be used to give information of the defect directly which will complement the information provided by micro Raman spectroscopy. Combination of Raman spectroscopy with TEM, STS and STM should be developed in the near future and will be powerful tools for defect characterization. Dynamic defect studies in the time domain should also yield valuable information. Regarding theory, we should consider in the future multi-scattering processes which modify the electronic density around a defect. The general formulation of elastic scattering matrix elements for different types of defects is another promising direction for future studies. Similar to the case of carbon nanotubes, where exciton effects are very important at room temperature, the disorder-induced features in nanographites should be considered within the excitonic picture and this approach may be significant for graphene samples with one and few layers.

Acknowledgements

The UFMG authors acknowledge the Brazilian Network on Carbon Nanotube Research and Instituto do Milênio de Nanotecnologia, CNPq, Brazil for partial support of this work. RS acknowledges a Grant-in-Aid (No. 16076201) from the Ministry of Education, Japan. The MIT authors acknowledge support under NSF Grants DMR 04-05538. The experiment shown in Fig. 4 was performed at Tuebingen University with the help of Prof. Achim Hartschuh and Ms Huihong Qian.

References

- 1 Y. Zhang, Y. W. Tan, H. L. Stormer and P. Kim, *Nature*, 2005, **438**, 197.
- 2 K. S. Novoselov, A. K. Geim, S. V. Morozov, D. Jiang, M. I. Katsnelson, I. V. Grigorieva, S. V. Dubonos and A. A. Firsov, *Nature*, 2005, **438**, 197–200.
- 3 R. Saito, G. Dresselhaus and M. S. Dresselhaus, *Physical Properties of Carbon Nanotubes*, Imperial College Press, London, 1998.
- 4 M. S. Dresselhaus, G. Dresselhaus, K. Sugihara, I. L. Spain and H. A. Goldberg, *Graphite Fibers and Filaments*, Vol. 5 of Springer Series in Materials Science, Springer-Verlag, Berlin, 1988.
- 5 M. S. Dresselhaus, G. Dresselhaus, R. Saito and A. Jorio, *Phys. Rep.*, 2005, **409**, 47–99.
- 6 L. G. Cançado, M. A. Pimenta, R. A. Neves, G. Medeiros-Ribeiro, T. Enoki, Y. Kobayashi, K. Takai, K. Fukui, M. S. Dresselhaus, R. Saito and A. Jorio, *Phys. Rev. Lett.*, 2004, **93**, 047403.
- 7 F. Tuinstra and J. L. Koenig, *J. Phys. Chem.*, 1970, **53**, 1126.
- 8 F. Tuinstra and J. L. Koenig, *J. Compos. Mater.*, 1970, **4**, 492.
- 9 P. Lespade, A. Marchand, M. Couzi and F. Cruege, *Carbon*, 1984, **22**, 375.
- 10 P. Lespade, R. Al-Jishi and M. S. Dresselhaus, *Carbon*, 1982, **20**, 427–431.
- 11 H. Wilhelm, M. Lelausian, E. McRae and B. Humbert, *J. Appl. Phys.*, 1998, **84**, 6552–6558.
- 12 A. C. Ferrari and J. Robertson, *Phys. Rev. B: Condens. Matter Mater. Phys.*, 2000, **61**, 14095.
- 13 L. G. Cançado, K. Takai, T. Enoki, M. Endo, Y. A. Kim, H. Mizusaki, A. Jorio, L. N. Coelho, R. Magalhães-Paniago and M. A. Pimenta, *Appl. Phys. Lett.*, 2006, **88**, 163106.
- 14 L. G. Cançado, K. Takai, T. Enoki, M. Endo, Y. A. Kim, H. Mizusaki, A. Jorio and M. A. Pimenta, 2006, submitted to APL.
- 15 L. G. Cançado, M. A. Pimenta, B. R. A. Neves, M. S. S. Dantas and A. Jorio, *Phys. Rev. Lett.*, 2004, **93**, 247401.
- 16 A. C. Ferrari, J. C. Meyer, V. Scardaci, C. Casiraghi, M. Lazzeri, M. Mauri, S. Piscanec, D. Jiang, K. S. Novoselov, S. Roth and A. K. Geim, *Phys. Rev. Lett.*, 2006, **97**, 187401.
- 17 D. Graf, F. Molitor, K. Ensslin, C. Stampfer, A. Jungen, C. Hierold and L. Wirtz, 2006, *arXiv:condmat/0607562v1*.
- 18 A. Gupta, G. Chen, P. Joshi, S. Tadigadapa and P. Eklund, *Nano Lett.*, 2006, **6**, 2667.
- 19 J. Klett, R. Hardy, E. Romine, C. Walls and T. Burchell, *Carbon*, 2000, **38**, 953.
- 20 E. B. Barros, N. S. Demir, A. G. Souza Filho, J. Mendes Filho, A. Jorio, G. Dresselhaus and M. S. Dresselhaus, *Phys. Rev. B: Condens. Matter Mater. Phys.*, 2005, **71**, 165422.
- 21 B. T. Kelly, *Physics of Graphite*, Applied Science (London), 1981.
- 22 G. G. Samsonidze, E. B. Barros, R. Saito, J. Jiang, G. Dresselhaus and M. S. Dresselhaus, *Phys. Rev. Lett.*, 2006.
- 23 J. Maultzsch, S. Reich, C. Thomsen, H. Requardt and P. Ordejon, *Phys. Rev. Lett.*, 2004, **92**, 075501.
- 24 K. A. Wang, A. M. Rao, P. C. Eklund, M. S. Dresselhaus and G. Dresselhaus, *Phys. Rev. B: Condens. Matter Mater. Phys.*, 1993, **48**, 11375–11380.
- 25 J. Jiang, R. Saito, G. G. Samsonidze, S. G. Chou, A. Jorio, G. Dresselhaus and M. S. Dresselhaus, *Phys. Rev. B: Condens. Matter Mater. Phys.*, 2005, **72**, 235408–1–11.
- 26 S. Piscanec, M. Lazzeri, M. Mauri, A. C. Ferrari and J. Robertson, *Phys. Rev. Lett.*, 2004, **93**, 185503.
- 27 M. S. Dresselhaus and G. Dresselhaus, *Adv. Phys.*, 1981, **30**, 139–326.
- 28 M. Endo, R. Ismail, T. Hiraoka, T. Karaki, T. Kasai, M. J. Matthews, S. D. M. Brown and M. S. Dresselhaus, in *Extended Abstracts of the 23rd Biennial Conference on Carbon*, Vol. II, ed. P. A. Thrower, American Carbon Society, Penn. State University, State College, PA, USA, 1997, p. 146.
- 29 I. L. Spain, K. J. Volin, H. A. Goldberg and I. Kalnin, *J. Phys. Chem. Solids*, 1983, **44**, 839.
- 30 M. S. Dresselhaus and G. Dresselhaus, *Adv. Phys.*, 2002, **51**, 1–186.
- 31 K. Sato, M. Noguchi, A. Demachi, N. Oki and M. Endo, *Science*, 1994, **264**, 556.
- 32 C. Kim, T. Fujino, T. Hayashi, M. Endo and M. S. Dresselhaus, *J. Electrochem. Soc.*, 2000, **147**, 1265–1270.
- 33 K. Nakada, M. Fujita, G. Dresselhaus and M. S. Dresselhaus, *Phys. Rev. B: Condens. Matter Mater. Phys.*, 1996, **54**, 17954–17961.
- 34 K. Sasaki, M. Murakami and R. Saito, *Appl. Phys. Lett.*, 2006, **88**, 113110.
- 35 Y. Niimi, T. Matsui, H. Kambara, K. Tagami, M. Tsukada and H. Fukuyama, *Appl. Surf. Sci.*, 2005, **241**, 43.
- 36 Y. Kobayashi, K. Fukui, T. Enoki, K. Kusakaba and Y. Kaburagi, *Phys. Rev. B: Condens. Matter Mater. Phys.*, 2005, **71**, 193406.
- 37 A. R. Badzian, P. K. Backmann, T. Hartnett, T. Badzian and R. Messier, in *Amorphous Hydrogenated Carbon Films*, ed. P. Koidl and P. Oelhafen, Les Editions de Physique, 1987, Vol. XVII, p. 67.
- 38 M. S. Dresselhaus and R. Kalish, *Ion Implantation in Diamond Graphite and Related Materials*, Springer-Verlag, Springer Series in Materials Science, Berlin, 1992.
- 39 M. Endo, Y. Kim, T. Hayashi, H. Muramatsu, M. Terrones, R. Saito, F. Villalpando, S. G. Chou and M. S. Dresselhaus, *Small*, 2006, **2**, 1031–1036.
- 40 C. Fantini, E. Cruz, A. Jorio, M. Terrones, H. Terrones, V. G. J.-C. Charlier, M. S. Dresselhaus, R. Saito, Y. A. Kim, T. Hayashi, H. Muramatsu, M. Endo and M. A. Pimenta, *Phys. Rev. B: Condens. Matter Mater. Phys.*, 2006, **73**, 193408–1–4.
- 41 D. Nishide, H. Dohi, T. Wakabayashi, E. Nishibori, S. Aoyagi, M. Ishida, S. Kikuchi, R. Kitaura, T. Sugai, M. Sakata and H. Shinohara, *Chem. Phys. Lett.*, 2006, in press.
- 42 A. Hartschuh, N. Anderson and L. Novotny, *J. Microsc.*, 2003, **201**, 234–240.
- 43 D. S. Knight and W. B. White, *J. Mater. Res.*, 1989, **4**, 385.
- 44 R. J. Nemanich and S. A. Solin, *Solid State Commun.*, 1977, **23**, 417.
- 45 R. J. Nemanich and S. A. Solin, *Phys. Rev. B: Condens. Matter Mater. Phys.*, 1979, **20**, 392–401.
- 46 R. P. Vidano, D. B. Fishbach, L. J. Willis and T. M. Loeher, *Solid State Commun.*, 1981, **39**, 341.
- 47 T. P. Mernagh, R. P. Cooney and R. A. Johnson, *Carbon*, 1984, **22**, 39–42.
- 48 M. Ramsteiner and J. Wagner, *Appl. Phys. Lett.*, 1987, **51**, 1355.
- 49 M. J. Matthews, M. A. Pimenta, G. Dresselhaus, M. S. Dresselhaus and M. Endo, *Phys. Rev. B: Condens. Matter Mater. Phys.*, 1999, **59**, R6585.
- 50 J. Kastner, T. Pichler, H. Kuzmany, S. Curran, W. Blau, D. N. Weldon, M. Dlamisier, S. Draper and H. Zandbergen, *Chem. Phys. Lett.*, 1994, **221**, 53.
- 51 I. Pócsik, M. Hundhausen, M. Koós and L. Ley, *J. Non-Cryst. Solids*, 1998, **227–230**, 1083–1086.
- 52 P. H. Tan, S. Dimovski and Y. Gogotsi, *Philos. Trans. R. Soc. London, Ser. A*, 2004, **362**, 2289.
- 53 R. Saito, A. Jorio, A. G. Souza Filho, G. Dresselhaus, M. S. Dresselhaus and M. A. Pimenta, *Phys. Rev. Lett.*, 2002, **88**, 027401.
- 54 A. V. Baranov, A. N. Bekhterev, Y. S. Bobovich and V. I. Petrov, *Opt. Spectrosc.*, 1987, **62**, 1036.
- 55 C. Thomsen and S. Reich, *Phys. Rev. Lett.*, 2000, **85**, 5214.
- 56 R. Saito, A. Grüneis, G. G. Samsonidze, V. W. Brar, G. Dresselhaus, M. S. Dresselhaus, A. Jorio, L. G. Cançado, C. Fantini, M. A. Pimenta and A. G. Souza Filho, *New J. Phys.*, 2003, **5**, 157.1–157.15.
- 57 L. G. Cançado, M. A. Pimenta, R. Saito, A. Jorio, L. O. Ladeira, A. Grüneis, A. G. Souza Filho, G. Dresselhaus and M. S. Dresselhaus, *Phys. Rev. B: Condens. Matter Mater. Phys.*, 2002, **66**, 035415.
- 58 K. Takai, M. Oga, H. Sato, T. Enoki, Y. Ohki, A. Taomoto, K. Suenaga and S. Iijima, *Phys. Rev. B: Condens. Matter Mater. Phys.*, 2003, **67**, 214202.
- 59 I. P. Batra and S. Ciraci, *J. Vac. Sci. Technol., A*, 1988, **6**, 313.
- 60 P.-H. Tan, Y.-M. Deng and Q. Zhao, *Phys. Rev. B: Condens. Matter Mater. Phys.*, 1998, **58**, 5435–5439.
- 61 Y. Kobayashi, K. Takai, K. Fukui, T. Enoki, K. Harigaya, Y. Kaburagi and Y. Hishiyama, *Phys. Rev. B: Condens. Matter Mater. Phys.*, 2004, **69**, 035418.
- 62 J. Jiang, R. Saito, A. Grüneis, S. G. Chou, G. G. Samsonidze, A. Jorio, G. Dresselhaus and M. S. Dresselhaus, *Phys. Rev. B: Condens. Matter Mater. Phys.*, 2005, **71**, 205420–1–13.

- 63 A. G. Souza Filho, N. Kobayashi, J. Jiang, A. Grüneis, R. Saito, S. B. Cronin, J. Mendes Filho, G. G. Samsonidze, G. Dresselhaus and M. S. Dresselhaus, *Phys. Rev. Lett.*, 2005, **95**, 217403.
- 64 K. Sato, R. Saito, Y. Oyama, J. Jiang, L. G. Cançado, M. A. Pimenta, A. Jorio, G. G. Samsonidze, G. Dresselhaus and M. S. Dresselhaus, *Chem. Phys. Lett.*, 2006, **427**, 117–121.
- 65 T. Ando, T. Nakanishi and R. Saito, *J. Phys. Soc. Jpn.*, 1998, **67**, 2857–2862.
- 66 T. Ando and T. Nakanishi, *J. Phys. Soc. Jpn.*, 1998, **67**, 1704.
- 67 G. G. Samsonidze, R. Saito, N. Kobayashi, A. Grüneis, J. Jiang, A. Jorio, S. G. Chou, G. Dresselhaus and M. S. Dresselhaus, *Appl. Phys. Lett.*, 2004, **85**, 5703–5705.
- 68 O. Dubay, G. Kresse and H. Kuzmany, *Phys. Rev. Lett.*, 2002, **88**, 235506.
- 69 C. Thomsen and S. Reich, *Phys. Rev. Lett.*, 2000, **85**, 5214.
- 70 Y. Wang, D. C. Aolmsmeyer and R. L. McCreery, *Chem. Mater.*, 1990, **2**, 557.



9050/090

RSCPublishing

**Fast
Publishing?**
Ahead of the field

To find out more about RSC Journals, visit

www.rsc.org/journals